Circularly Polarized THz Wave Generation Using Graphene Nanostructures

François Aguillon, Andrei G Borisov

To cite this version:

François Aguillon, Andrei G Borisov. Circularly Polarized THz Wave Generation Using Graphene Nanostructures. Journal of Physical Chemistry C, 2025, ⟨10.1021/acs.jpcc.5c06110⟩. ⟨hal-05422666⟩

Circularly Polarized THz Wave Generation Using Graphene Nanostructures

François Aguillon* and Andrei G. Borisov*

Institut des Sciences Moléculaires d'Orsay (ISMO), UMR 8214, CNRS, Université Paris-Saclay, 91405 Orsay Cedex, France.

E-mail: francois.aguillon@universite-paris-saclay.fr; andrei.borissov@universite-paris-saclay.fr

Phone: +33 (0)1 69157697

Abstract

Building on the strong nonlinear response of graphene nanostructures and Neumann's symmetry principle, we theoretically study the difference-frequency generation (DFG) of a circularly polarized THz field with controllable handedness (or spin angular momentum, SAM). Using the tight-binding description of graphene and the time-dependent density matrix approach, we perform real-time calculations of the nonlinear conversion produced by the interaction of the two contra-rotating, circularly polarized infrared electromagnetic pulses with individual graphene nanoflakes and nanoribbon compounds. We observe high conversion efficiency for all studied systems, as evidenced by their performance when arranged into the metasurface. In such configurations, the efficiency of the DFG of the SAM-carrying THz field can be above 10^{-3} W/W^2. We further address the possibility of mitigating the effects of the unavoidable in practical situations symmetry distortions at the atomic or macroscopic level, which degrade the SAM selectivity of DFG. Our work extends theoretical studies of the THz manipulation with graphene nanomaterials towards spin-carrying radiation.

Introduction

Nowadays, THz technologies are experiencing rapid expansion in various fields of fundamental and applied research, ranging from sensors, imaging, and communications[1–6] to near-field imaging[6–8] and scanning tunneling probes. In this latter situation, directing the THz pulses into the junction of a scanning tunneling microscope allows one to track with atomic-scale resolution the dynamics of molecular vibrations, electron transfer, and electron-photon coupling.[6,9–16] This is without mentioning the possibility of using THz radiation for controlling electron emission by ultrashort and powerful optical pulses.[17] The progress of the field would benefit from the development of compact THz sources. To this end, along with the utilization of the quantum cascade lasers,[5,6] 2D materials and in particular graphene appear as a promising platform.[18–21] owing to their high and tunable nonlinearity[22–34] associated among other effects with collective electron excitations (plasmons).[35–38] Thus, along with THz generation in graphene by the photon drag effect,[39,40] carrier injection at graphene-metal interfaces,[41] and a photoconductive switch approach,[42] the generation of THz graphene plasmons using the nonlinear difference frequency generation (DFG) has been reported.[43–45]

The application range of THz technology can be further extended by using (nonlinear) metasurfaces for engineering THz radiation carrying spin and orbital momentum. This said, while manipulation and generation of structured light with nonlinear metasurfaces have benefitted from extensive theoretical and experimental research at optical frequencies,[46–58] the THz frequency range is much less studied so far.[59–61]

In this theoretical work we leverage the high nonlinearity of graphene nanostructures to obtain circularly polarized (carrying spin angular momentum, SAM) THz radiation via the DFG process. Since an individual graphene nanostructure can be seen as a meta-atom or building block of the 2D metasurface, characterizing its nonlinear response is a necessary step for further developments. Using Neumann's symmetry principle,[62,63] and an approach similar to that employed for circular polarization states of the high harmonic generation,[56–58,64–68] we define conditions to control the circular polarization states of THz radiation obtained by

DFG in graphene nanostructures. We then apply the time-dependent density matrix approach and tight-binding description of graphene (TDDM-TB) to calculate the electron density dynamics in graphene triggered by the two contra-rotating circularly polarized infrared pulses, and to characterize the dipole induced in the nanostructure at THz frequencies. From the perspective of practical applications, we further address the role of symmetry breaking by atomic-scale or geometry imperfections, which strongly degrade the SAM selectivity of the process. Similar to our earlier findings for high-harmonic generation,[68] we show that this problem can be alleviated when individual nanostructures are arranged into a metasurface.

The paper is organized as follows. The first section provides a brief description of the method and defines conditions for the incident electromagnetic waves necessary for the DFG of SAM-carrying THz radiation. The second section describes the TDDM-TB results obtained for ideal and defective triangular graphene nanoflakes. The third section is devoted to the TDDM-TB results obtained for ideal and defective compound structures made of several (centrosymmetric or not) graphene nanoribbons (GNRs), as well as for a disordered array of such compounds.

Unless otherwise stated, atomic units are used throughout the paper.

Method

The nonlinear response of graphene nanostructures, and in particular the DFG process $\Omega = \omega_1 - \omega_2$ leading to THz generation, which is the focus of this work, is studied using the explicitly time-dependent TDDM-TB approach presented in detail elsewhere[69] and summarized in the supporting information (SI) of the present manuscript (see also Refs. 70,71). In brief, our method builds on earlier theoretical developments to address linear and nonlinear effects in graphene plasmonics.[72,73] It is based on the time-dependent density-matrix (TDDM) calculations of the electron density dynamics in the π-bands of graphene nanoflakes described using the tight-binding (TB) model. The time-dependent density matrix, $\hat{\rho}(t)$, is represented in the basis φ_ν of the carbon $2p_z$ orbitals, which are centered at the carbon atom sites within the nanostructure

$$\hat{\rho}(t) = \sum_{\nu,\nu'} |\varphi_\nu\rangle \rho_{\nu,\nu'}(t) \langle \varphi_{\nu'}|, \quad \varphi_\nu(\mathbf{r}) = \varphi_{2p_z}(\mathbf{r} - \mathbf{R}_\nu). \tag{1}$$

where $\mathbf{R}_\nu$ denotes the position of the carbon atom site ν and $\mathbf{r}$ represents electron coordinates. The time evolution of $\hat{\rho}(t)$ is given by the quantum master equation[74–76]

$$i\frac{\partial \hat{\rho}(t)}{\partial t} = \left[\hat{H}, \hat{\rho}(t)\right] - i\gamma \left(\hat{\rho}(t) - \hat{\rho}^{(0)}\right). \tag{2}$$

Eq. (2) is solved in real time using the split-operator technique,[77] with the initial condition for time-propagation given by $\hat{\rho}(t = 0) = \hat{\rho}^{(0)}$, where $\hat{\rho}^{(0)}$ is the density matrix of the ground-state system.

The TB hamiltonian $\hat{H} = \widehat{H^{(0)}} + \hat{V}(t)$ comprises the hamiltonian of the unperturbed ground-state system, $\hat{H}^{(0)}$, and the potential $\hat{V}(t)$, which is created by the incident electromagnetic radiation and by the induced electron density (i.e., the electron density change with respect to the ground-state reference density, $\rho_{\nu\nu}(t) - \rho^{(0)}_{\nu\nu}$). Retardation effects are neglected because of the small relevant size of the considered systems. The hamiltonian of the ground-state system is given by $\hat{H}^{(0)} = \sum_{\nu,j} |\varphi_\nu\rangle h \langle\varphi_j| + \hat{V}^{(0)}$, where j stands for the nearest neighbours of ν, and the hopping integral $h = -2.8$ eV.[36] The potential $\hat{V}^{(0)}$ stems from the deviation from the homogeneous charge distribution of the infinite graphene layer because of the finite size of the nanoflakes and their electrostatic doping.

The second term on the right-hand-side of Eq. (2) is a simplified form of the Lindblad super-operator and it describes the relaxation to the ground-state density matrix $\hat{\rho}^{(0)}$ with a rate γ. Here, in line with other works,[26,78] we use $\gamma = 15$ meV to represent the plasmon decay by the excitation of the optical phonons in graphene.[35,79–82] The Landau damping of plasmons by edge and defect scattering[82–85] is implicitly accounted for in the TDDM-TB framework. It is worth noting that as discussed below, the qualitative conclusions of this work regarding SAM selectivity of DFG are determined by the symmetry of the system and are therefore robust with respect to the choice of γ.

We consider the situation sketched in Figure 1a. Two incident circularly polarized electromagnetic waves (denoted as 1 and 2), with electric field vectors $\mathbf{E}_1$ and $\mathbf{E}_2$, and frequencies ω_1 and ω_2, propagate in positive direction of z-axis. That is, the propagation direction is perpendicular to the graphene nanoflake located in the (xy)-plane. The symmetry selection rules for nonlinear multipoles induced in this situation in the graphene nanostructure are thoroughly derived and explained in the SI. Although below in this paper we will show an alternative approach, our main derivation reported in the SI is based on Neumann's principle which requires that the tensor that determines the response of the nanostructure is invariant under transformation respecting the symmetry of the nanostructure[62,63] (for the high harmonic generation see discussion in Refs.[56–58,64–67]). In particular, for the DFG, the polarization states $\mu_{\mathrm{THz}} = \pm 1$ of the nonlinear dipole $\mathbf{p}(\Omega)$ induced in the nanostructure at THz frequency $\Omega = \omega_1 - \omega_2$ can be obtained from (we consider that the frequencies are positive)

$$\mu_1 - \mu_2 - \mu_{\mathrm{THz}} = n\ \mathcal{S}. \tag{3}$$

Here $\mathcal{S}$ is the order of the rotational symmetry of the graphene nanoflake, n is any integer, and $\mu_{1,2} = \pm 1$ is the spin angular momentum (SAM, or handedness) of the fundamental electromagnetic field $\mathbf{E}_{1,2}$. We use $\mu_{1,2} = +1$ for the circular polarization with a counterclockwise rotation of the electric field vector in the graphene plane (the left-handed polarization), and $\mu_{1,2} = -1$ for the circular polarization with a clockwise rotation of the field vector in the graphene plane (the right-handed polarization). Similarly, $\mu_{\mathrm{THz}} = +1$ ($\mu_{\mathrm{THz}} = -1$) corresponds to a counterclockwise (clockwise) rotation of the induced nonlinear dipole in the graphene plane.

From Eq. (3) it follows that the *only* way to create a SAM selective DFG is to choose an individual nanoflake or a compound system of several nanoflakes with C3 symmetry ($\mathcal{S} = 3$)

illuminated by two contra-rotating optical fields, i.e.,

$$\mu_1 = \pm 1, \quad \mu_2 = -\mu_1, \quad \mathcal{S} = 3. \tag{4}$$

This results in the circularly polarized far field THz radiation emitted perpendicular to the graphene plane with

$$\mu_{\mathrm{THz}} = \mu_2 = -\mu_1. \tag{5}$$

We thus set the incident electromagnetic waves with frequencies $\omega_1 > \omega_2$ leading to the sought DFG in the following form in graphene plane

$$\mathbf{E}_j(t) = E_0(t)\ \left(\hat{e}_x\ \cos\omega_j t + \hat{e}_y\ \mu_j \sin\omega_j t\right), \tag{6}$$

Here, the unit length vector along the x-axis (the y-axis) is denoted as $\hat{e}_x$ ($\hat{e}_y$), polarizations of the incident waves are $\mu_1 = -1$, and $\mu_2 = +1$, and the slowly varying amplitude $E_0(t)$ is common to both fields. It is given by

$$E_0(t) = A_0\ \exp\left[-\left(\frac{t - t_0}{\tau}\right)^2\right]. \tag{7}$$

Since the nonlinear response of the graphene nanostructure and, in particular the DFG is strongly enhanced at plasmon resonances,[26] we used ω_1 and ω_2 given by

$$\omega_1 = \omega_{\mathrm{DP}} + \Omega/2 \quad \text{and} \quad \omega_2 = \omega_{\mathrm{DP}} - \Omega/2 \quad \text{where} \quad \Omega = 30\ \text{meV}\ \approx 7\ \text{THz}. \tag{8}$$

Here, ω_{DP} is the frequency of the dipolar plasmon resonance of the nanostructure. The pulse duration (FWHM of the field), $\tau = 3 \times 10^4$ a.u. (≈ 726 fs), is chosen such that it comprises approximately 5 periods of the THz field. The solution of Eq. (2) is computed within the time interval $0 \le t \le t_{max}$. By setting $t_0 = 5 \times 10^4$ a.u. (≈ 1210 fs) and $t_{max} = 1.1 \times 10^5$ a.u. (≈ 2660 fs), we ensure that (i) the incoming pulse is negligible in the beginning and at the end of the time-propagation, and (ii) the induced density fully relaxes to the ground state by the end of the time propagation.

From the time-dependent electron density induced in the graphene nanostructure by the incident electromagnetic field, and calculated using the TDDM-TB method, we obtain the time-dependent induced dipole $\mathbf{p}(t) = \sum_\nu \left(\rho_{\nu\nu}(t) - \rho_{\nu\nu}^{(0)}\right) \mathbf{R}_\nu$. We then perform its frequency analysis according to

$$\mathbf{p}(\omega) = \frac{1}{\sqrt{2\pi}} \int_{-\infty}^{\infty} \mathbf{p}(t)\, e^{i\omega t}\, \mathrm{d}t. \tag{9}$$

The frequency-resolved dipole $\mathbf{p}(\omega)$ is represented in the basis of rotating vectors

$$\mathbf{p}(\omega) = \hat{e}_+\, p_+(\omega) + \hat{e}_-\, p_-(\omega) \qquad \text{with} \qquad \hat{e}_\pm = \frac{1}{\sqrt{2}}(\hat{e}_x \pm i\hat{e}_y). \tag{10}$$

The left- and right-handed (complex) polarisation amplitudes $p_\pm(\omega)$ provide a complete description of the linear and nonlinear response of the system.

Thus, we define the polarization index $\mathcal{I}_p(\omega)$

$$\mathcal{I}_p(\omega) = \frac{|p_+(\omega)| - |p_-(\omega)|}{|p_+(\omega)| + |p_-(\omega)|}, \tag{11}$$

it is $+1$ (-1) if the dipole is purely left- (right-) handed, and it is 0 if the dipole is linearly polarized. In what follows, we will be mainly interested in $\mathcal{I}_p(\Omega)$ which characterizes the DFG at $\Omega \;=\; \omega_1 - \omega_2$. One can also define the second order hyperpolarizabilities

$$\alpha_\pm^{(2)}(\Omega) = \frac{|p_\pm(\Omega)|}{|\mathbf{E}_1(\omega_1)|\, |\mathbf{E}_2(\omega_2)|}, \tag{12}$$

where $\mathbf{E}_j(\omega)$ is obtained from $\mathbf{E}_j(t)$ using the same time-to-frequency transform (see Eq. (9)).

The far field THz emission by the free-standing nanostructure can be found from[86]

$$\mathbf{E}_{\mathrm{THz}}(\mathbf{r}, \Omega) = k^2\, \frac{e^{ikr}}{r}\, (\hat{e}_r \times \mathbf{p}(\Omega)) \times \hat{e}_r, \tag{13}$$

where $\mathbf{r} = (x, y, z)$, the unit length vector $\hat{e}_r = \frac{\mathbf{r}}{r}$, and wavevector $k = \Omega/c$ (c is the speed of light in vacuum). In particular, the emission along the z-axis perpendicular to the graphene plane is given by

$$\mathbf{E}_{\text{THz}}(\mathbf{r}, \Omega) = k^2 \, \frac{e^{ikz}}{z} \left(\hat{e}_+ \; p_+(\Omega) + \hat{e}_- \; p_-(\Omega) \right). \tag{14}$$

That is, the polarization of the THz radiation emitted in the direction of propagation of the fundamental waves $\mathbf{E}_1$ and $\mathbf{E}_2$ is the same as that of the nonlinear dipole induced at the difference frequency. In what follows, we will consider this situation relevant for the response of nonlinear metasurfaces composed of graphene nanostructures to fundamental wave(s) at normal incidence. Consequently, by DFG we will understand the far-field radiation at THz frequency Ω emitted along the z-axis perpendicular to graphene. Thus, the symmetry selection rules derived for polarization states μ_{THz} of the nonlinear dipole $\mathbf{p}(\Omega)$ and given by Eq. (3), Eq. (4), and Eq. (5) also describe the polarization states of the DFG.

We explicitly checked that for the variation of the electric field amplitude A_0 between 10^{-6} and 10^{-5} a.u. the perturbative regime holds, i.e., $\alpha^{(2)}_{\pm}(\Omega)$ is independent of A_0 as we further show in SI. This also points at the dominance of the second order nonlinear process, and the absence of notable transient effects linked with electron heating.[78,87] For numerical convenience, we then used $A_0 = 10^{-5}$ a.u. (5×10^{-3} V/nm) throughout this work.

THz generation by the triangular nanoflake

We start our discussion with an example of the DFG by a triangular graphene nanoflake with perfect $\mathcal{S} = 3$ symmetry, sketched in Fig. 1a. It comprises 10194 C atoms and has armchair 469 a.u. long edges (approximately 25 nm). The tips of the nanoflake are smoothed with a 1 nm curvature radius. We neglect the relaxation of the carbon atoms at the boundaries of the nanostructure as it does not affect the symmetry and produces only a minor effect on the nonlinear response.[68] The nanoflake is electrostatically doped with 20 electrons so that its dipolar plasmon frequency $\omega_{\text{DP}} = 0.236$eV, as evidenced by the resonance in the

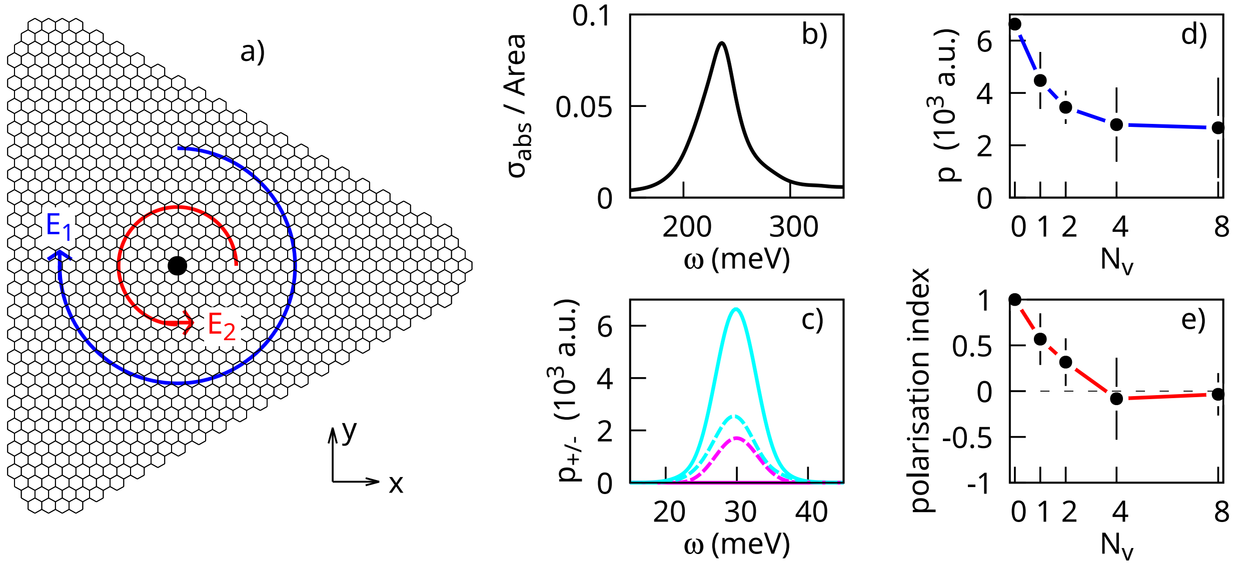

Figure 1: The DFG of the THz radiation from the triangular graphene nanoflake described in the text. The nonlinear response is induced by two contra-rotating circularly polarized electromagnetic pulses with electric field vector $\mathbf{E}_1$, frequency $\omega_1 = 251$ meV, and $\mu_1 = -1$ polarization for the first pulse, and with electric field vector $\mathbf{E}_2$, frequency $\omega_2 = 221$ meV, and $\mu_2 = +1$ polarization for the second pulse. **Panel a:** sketch of the triangular graphene nanoflake and of the direction of rotation of the electric field vectors $\mathbf{E}_1$ and $\mathbf{E}_2$. The black point is the center of the C3 symmetry. For the sake of visibility of the graphene lattice, the nanoflake presented here is 5 times smaller than the one used in the calculation. **Panel b:** optical absorption cross section, σ_{abs}, normalized to the area of the graphene nanoflake. The data is shown as a function of the frequency ω of the x-polarized optical pulse. It features a resonance at the dipolar plasmon frequency $\omega_{\mathrm{DP}} = 0.236$eV. **Panel c:** left handed ($|p_+|$, cyan) and right handed ($|p_-|$, magenta) nonlinear dipolar polarization amplitudes defined with Eq. (10). Results are shown as a function of frequency ω within the frequency range near DFG at $\Omega = \omega_1 - \omega_2 = 30$ meV. Full lines: results for perfect triangular nanoflake; Dashed lines: defective nanoflake containing a single carbon atom vacancy. **Panel d:** the amplitude of the nonlinear dipole $|\mathbf{p}(\Omega)|$. **Panel e:** polarization index $\mathcal{I}_p(\Omega)$ defined with Eq. (11). In panels d) and e) results at the difference frequency $\Omega = 30$ meV are shown as a function of the number of randomly distributed carbon atom vacancies $\mathrm{N_v}$. The error bars show the standard deviation.

absorption spectra in Fig. 1b. The DFG is induced by two incident contra-rotating circularly polarized optical pulses with electric field vectors $\mathbf{E}_1$ and $\mathbf{E}_t$, frequencies $\omega_1 = 251$ meV and $\omega_2 = 221$ meV, and SAM $\mu_1 = -1$ and $\mu_2 = +1$. The direction of the rotation of the electric field vectors in the plane of the nanoflake is indicated in Fig. 1a, and the pulse profile and field amplitude are described in the previous section.

The TDDM-TB results for an ideal nanoflake, as shown in Fig. 1c are in full accord with selection rules for circularly polarized states of the DFG. Indeed, as predicted by Eq. (4) and Eq. (5), the DFG is SAM-selective. The nonlinear dipole induced at THz frequency is purely left-handed with SAM $\mu_{\mathrm{THz}} = \mu_2 = +1$. The spectral width of the THz signal is consistent with the spectral width of the incoming fields (a few meV) and the relaxation rate $\gamma = 15$ meV introduced in Eq. (2) to represent the interaction with optical phonons.

While the results for an ideal nanoflake demonstrate the sought possibility of the DFG of the circularly polarized THz pulse with controllable handedness, the question naturally arises regarding the robustness of the results with respect to the lattice imperfections. Indeed, lattice imperfections unavoidably destroy the atomic-scale C3 symmetry of the nanostructure and affect the selection rules for the circular polarization of the nolinear dipole.[68] To access the role of the defects, we consider single carbon atom vacancies in the nanoflake. We follow a widely used approach[88–91] where several randomly chosen carbon atoms are removed from an ideal graphene lattice and the lattice relaxation around defects is neglected. In our earlier works[68,69] we compared this simple model with *ab initio* fully-relaxed descriptions of the defects,[92–95] and we have demonstrated that the former yields semi-quantitative results for the nonlinear response of defective graphene nanostructures.

Strictly speaking, even a unique defect downgrades the symmetry order of the nanoflake from $\mathcal{S} = 3$ to $\mathcal{S} = 1$. In this situation, it follows from Eq. (3) that the induced dipole will be generated with both polarizations $\mu_{\mathrm{THz}} = \pm 1$ when $\mu_2 = -\mu_1$. Thus, the SAM selectivity of the nonlinear process is lost. This said, for the unique vacancy out of 10^4 carbon atoms the distortion of the perfect nanostructure is small, it is on the atomic scale. The symmetry given by the macroscopic geometry of the nanoflake is preserved. Naively one might expect that the induced THz dipole remains almost left-handed. This is absolutely not the case as illustrated in Fig. 1c. Both nonlinear polarizations are produced with similar intensity (results shown with dashed lines). The loss of handedness selectivity caused by a unique carbon atom vacancy present in the honeycomb lattice is spectacular.

To further explore the role of the defects we computed the THz generation from triangular nanoflakes with $\mathrm{N_v} = 1, 2, 4,$ and 8 carbon atom vacancies. For each $\mathrm{N_v}$ we generated five defective nanoflakes with random carbon atom vacancy positions. We present in Fig. 1d the statistically averaged results for the nonlinear dipole $\mathbf{p}(\Omega)$, and in Fig. 1e for the polarization index $\mathcal{I}_p(\Omega)$ at the THz frequency $\Omega = 30$ meV. The effect of the lattice imperfections on the DFG obtained here is similar to the one reported earlier for the generation of the circularly polarized harmonics of the fundamental frequency.[68] First, for $0 \leq \mathrm{N} =\leq 4$ the induced nonlinear dipole decreases with increasing number of vacancy defects leading to smaller THz emission into the far field. This is a consequence of the decay and dephasing of the dipolar plasmon of the nanoflake because of the electron scattering by defects.[79,81,83,84,96–98] Above four defects $|\mathbf{p}(\Omega)|$ varies only mildly on the scale of the figure and within the studied range of $\mathrm{N_v}$. Most important, already four randomly distributed carbon atom vacancies present in the nanostructure (defect concentration $\approx 4\times10^{-4}$) lead to the polarization index $\mathcal{I}_p(\Omega)$ close to zero. The sought generation of the circularly polarized THz radiation is lost. Obviously, a larger number of $\mathrm{N_v}$ can only further degrade the symmetry, so that we limited our study to $\mathrm{N_v} = 8$. These results point at the practical difficulty in implementing individual nanoflakes for SAM-controllable THz generation in the far field because of the extreme sensitivity of the DFG to the lattice symmetry on the atomic scale.

DFG using graphene nanoribbons

Centrosymmetric nanoribbons

Chemically synthesized in a bottom-up approach, GNRs possess perfect microscopic regularity[99–102] and thus represent an interesting alternative to large-size nanoflakes for SAM-controllable THz generation. With this in mind, we consider DFG generation by the C3 compound structure shown in Fig. 2a and in Fig. 2b. This structure consists of three identical GNRs radially disposed around a center of symmetry, with a rotation angle of $2\pi/3$

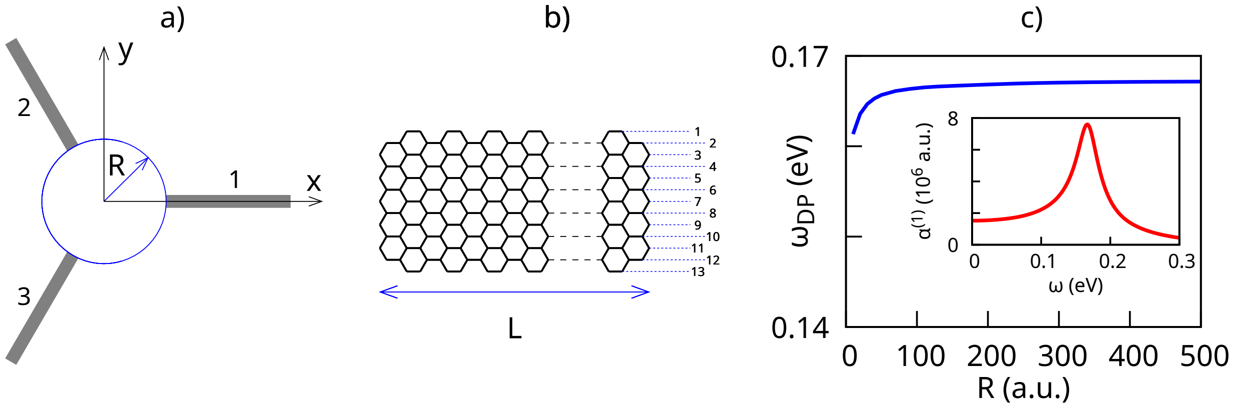

Figure 2: The C3 compound of the three identical GNRs. **Panel a:** geometrical arrangement of radially disposed GNRs with an angle $2\pi/3$ between them. R is the distance between the inner end of the nanoribbons and the center of symmetry of the compound ($R = 150$ a.u. is shown here). **Panel b:** arrangement of carbon atoms within the aGNR13 nanoribbon. The nanoribbon has a length of $L = 396$ a.u. and contains 1270 carbon atoms. The blue dashed lines indicate the carbon atom rows, labeled by $1, ..., 13$. **Panel c:** The frequency of the dipolar plasmon of the C3 compound of aGNR13 nanoribbons. Results are shown as a function of the geometry parameter R. The inset shows the linear dipolar polarizability $\alpha^{(1)}$ of the compound structure with $R = 400$ a.u.. It is calculated as a function of the frequency of the linearly polarized electromagnetic plane wave, and it reveals a dipolar plasmon resonance at $\omega_{\text{DP}} = 167$ meV.

between them. To reduce plasmon damping by edge scattering we have chosen GNRs with armchair edges.[85] Their width of 28 a.u. (approximately 1.5 nm) is such that they count 13 “horizontal” alignments of carbon atoms. These are the so-called aGNR13 nanoribbons[99–102] which exhibit semiconducting character and a highly non-linear response (see SI). Each aGNR13 nanoribbon considered here has a length of $L = 396$ a.u. (approximately 20.7 nm) and contains 1270 carbon atoms. Each nanoribbon is electrostatically doped with 6 electrons, resulting in a longitudinal dipolar plasmon frequency of an individual nanoribbon $\omega_{\text{DP}}^{\text{aGNR13}} = 167$ meV. Within the range of the geometry parameter R addressed here, 20 a.u. $\leq R \leq$ 500 a.u., the dipolar plasmon frequency of the GNRs compound changes only weakly, remaining close to $\omega_{\text{DP}}^{\text{aGNR13}}$, as shown in figure Fig. 2c.

The DFG from the C3 compound of aGNR13 nanoribbons is shown in Fig. 3. The non-linear response is induced by two contra-rotating circularly polarized electromagnetic pulses one with $\omega_1 = 182$ meV and $\mu_1 = -1$, and the other one with $\omega_2 = 152$ meV and $\mu_2 = +1$.

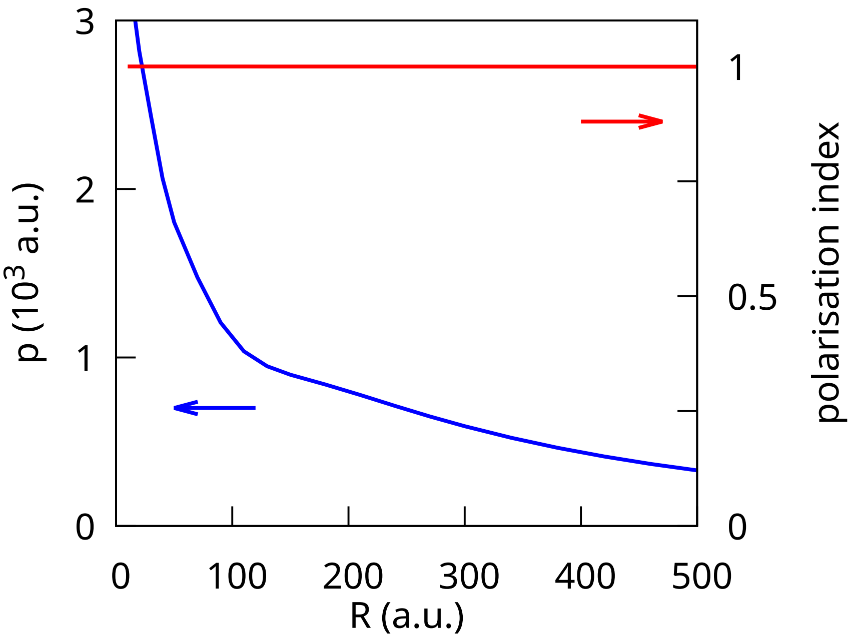

Figure 3: TDDM-TB results for the DFG generation from the C3 compound of identical aGNR13 graphene nanoribbons. The nonlinear response is induced by two contra-rotating circularly polarized electromagnetic pulses one with $\omega_1 = 182$ meV and $\mu_1 = -1$, and the other one with $\omega_2 = 152$ meV and $\mu_2 = +1$. The amplitude $|\mathbf{p}(\Omega)|$ (blue line, left vertical axis), and polarization index $\mathcal{I}_p(\Omega)$ of the induced nonlinear dipole (red line, right vertical axis) are shown at the difference frequency $\Omega = 30$ meV as a function of the geometry parameter R (see Fig. 2a).

The amplitude $|\mathbf{p}(\Omega)|$ (blue line), and the polarization index $\mathcal{I}_p(\Omega)$ (red line) of the induced nonlinear dipole at the difference frequency $\Omega = 30$ meV are calculated with TDDM-TB as a function of the geometry parameter R. In accord with the selection rules for the C3 symmetry (Eq. (4), and Eq. (5) we obtain that $\mathcal{I}_p(\Omega) = 1$ irrespective of R. The amplitude of the nonlinear dipole, on the other hand, rapidly decreases with R. Indeed, each individual aGNR13 nanoribbon considered here is centrosymmetric so that even-order hyperpolarizabilities are zero. Since only even-order nonlinear response enables DFG at $\Omega = \omega_1 - \omega_2$, THz generation is impossible for the free-standing nanoribbon. In contrast, in a compound nanostructure, the mutual interactions induce a non-centrosymmetric environment for each aGNR13 nanoribbon. This allows for even-order non linear effects. Obviously, when R increases the interactions between GNRs become smaller leading to the smaller $|\mathbf{p}(\Omega)|$ created by the compound. Except when explicitly mentioned, results presented below in this paper are obtained for $R = 50$ a.u. (≈ 2.6 nm). This choice is a compromise between the efficiency of frequency conversion and a realistic scale for constructing the compound.

If the bottom-up process ensures a perfect regularity of the nanoribbons at the atomic scale, defects may occur in the macroscopic geometry of the compound nanostructure. To access the role of these geometry distortions on the generation of THz radiation with controlled SAM, we addressed the defective aGNR13 compounds. Results shown in Fig. 4 are obtained by altering the position (δx, δy displacements), orientation ($\delta\varphi$ rotation) and length (δL elongation) of the aGNR13 nanoribbon labelled as 1 in Fig. 2a. The geometry distortion parameters δx, δy, $\delta\varphi$, and δL are defined in the insert of Fig. 4a. An ideal C3 compound corresponds to $R = 50$ a.u., $L = 396$ a.u., and a $2\pi/3$ angle between the nanoribbons.

The geometry distortions lift the C3 symmetry ($\mathcal{S} = 3$) and lead to a C1 symmetry ($\mathcal{S} = 1$) of the compound, so that one envisions the same consequences as those calculated for the defective triangular nanoflake in Fig. 1. Indeed, it follows from Fig. 4 that the symmetry break impacts the absolute value $|\mathbf{p}(\Omega)|$ (blue line), and the polarization index $\mathcal{I}_p(\Omega)$ (red line) of the nonlinear dipole induced at the difference frequency $\Omega = 30$ meV. Clearly, the sensitivity to defects already observed for the unique triangular nanoflake is present. Note however, that in the case of the triangular nanoflake, the symmetry break results from atomic-scale defects. The macroscopic geometry characterized by the C3 symmetry is preserved. In contrast, for the defective aGNR13 compound, the atomistic structure of the GNRs is preserved, and the distortions concern the macroscopic geometry. Thus, the atomic scale relevant for the triangular nanoflake transforms to the nanometer scale for the aGNR13 compound (100 a.u. ≈ 5.3 nm) with much better persistence of the polarization index in the latter system.

To get deeper insights into the performance of the compound system and into the possible ways of its improvement presented below, it is handy to go beyond the general framework provided by Neumann's principle. Let us establish the selection rules for the circular states

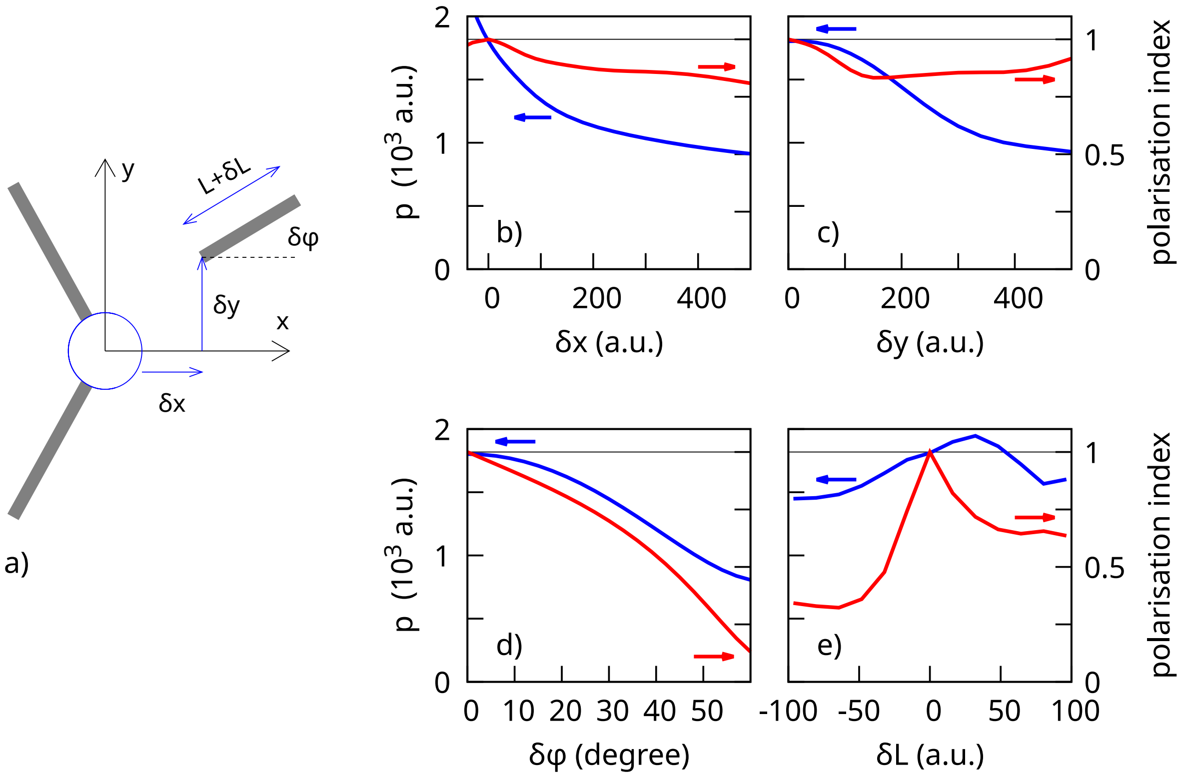

Figure 4: Effect of geometry distortion on the DFG from the compound structure of aGNR13 graphene nanoribbons. The nonlinear response is induced by two contra-rotating circularly polarized electromagnetic pulses one with $\omega_1 = 182$ meV and $\mu_1 = -1$, and the other one with $\omega_2 = 152$ meV and $\mu_2 = +1$. **Panel a:** geometry distortion parameters δx, δy, $\delta\varphi$, and δL describing displacement and elongation of the GNR oriented along the x-axis (nanoribbon 1 in Fig. 2a). The compound of ideal C3 symmetry corresponds to $R = 50$ a.u., $L = 396$ a.u., and zero distortion. **Panels b to e:** amplitude $|\mathbf{p}(\Omega)|$ (blue line, left vertical axis), and the polarization index $\mathcal{I}_p(\Omega)$ (red line, right vertical axis) of the induced nonlinear dipole. Results at the difference frequency $\Omega = 30$ meV are shown as a function of one of the distortion parameters, while the other distortion parameters are maintained at zero. **Panel b:** the nanoribbon is shifted in the xy plane by $\hat{e}_x\delta x$. **Panel c:** the nanoribbon is shifted in the xy plane by $\hat{e}_y\delta y$. **Panel d:** the nanoribbon is rotated by $\delta\varphi$. **Panel e:** length of the nanoribbon is changed to $L + \delta L$.

of the DFG that explicitly exploit the geometry of the compound structure addressed here. As explained above, while an individual aGNR13 nanoribbon is centrosymmetric, mutual interactions between nanoribbons allow for even-order nonlinear effects. The nonlinear dipole at the difference frequency is then induced in each GNR (given the aGNR13 geometry, the nonlinear dipole is aligned with the GNR axis). For the compound of three nanoribbons rotated by a $2\pi/3$ angle with respect to each other, and arranged as sketched in Fig. 2a, the unit vectors $\hat{e}_k$ ($k = 1, 2, 3$) in the radial direction along the nanoribbons are given by

$$\hat{e}_1 = \frac{\hat{e}_+ + \hat{e}_-}{\sqrt{2}} \qquad \hat{e}_2 = \frac{e^{-\frac{2i\pi}{3}}\ \hat{e}_+ + e^{\frac{2i\pi}{3}}\ \hat{e}_-}{\sqrt{2}} \qquad \hat{e}_3 = \frac{e^{\frac{2i\pi}{3}}\ \hat{e}_+ + e^{-\frac{2i\pi}{3}}\ \hat{e}_-}{\sqrt{2}} \tag{15}$$

Then, using the C3 symmetry, the THz dipoles induced in the nanoribbons at the frequency Ω can be expressed in the form

$$\mathbf{p}_k(\Omega) = p(\Omega)\ \exp(-i2\varphi_k)\ \hat{e}_k. \tag{16}$$

In Eq. (16) φ_k is the angle between nanoribbon k and the x-axis. In the present compound system, $\varphi_k = 2\pi(k-1)/3$. The $-2\varphi_k$ dephasing term arises from the time shift of the fields experienced by nanoribbon k because of its radial rotation by an angle φ_k in the compound system.

Indeed, let us consider for simplicity an incident cw radiation. The incident field of electromagnetic wave 1 rotates clockwise in the (x, y)-plane ($\mu_1 = -1$). Therefore, for nanoribbon k it is advanced by $\Delta t_{1,k} = \varphi_k/\omega_1$. Then, the radial component of the total field (incident field plus the field induced by the linear response of the nanostructure) as seen by nanoribbon k can be expressed as $\mathcal{E}_{1,k}(\omega_1) = \mathcal{E}_1(\omega_1)\ e^{-i\varphi_k}$ Conversely, the field of the electromagnetic wave 2 with $\mu_2 = +1$ is delayed by $\Delta t_{2,k} = \varphi_k/\omega_2$. As seen by the nanoribbon k the radial component of the corresponding total field can be expressed as $\mathcal{E}_{2,k}(\omega_2) = \mathcal{E}_2(\omega_2)\ e^{i\varphi_k}$ (notice that $\mathcal{E}_{1,k}$ and $\mathcal{E}_{2,k}$ depend on the position along the nanoribbon). The longitudinal polarization density at the difference frequency is given by $\mathcal{P}_k(\Omega = \omega_1 - \omega_2) \propto \mathcal{E}_{1,k}(\omega_1)\mathcal{E}^*_{2,k}(\omega_2)$, which leads to Eq. (16). (Here Z^* denotes the complex conjugate of Z.)

The total dipole induced in an ideal C3-symmetric aGNR13 compound at the difference frequency Ω is

$$\mathbf{p}_{\mathrm{comp}}(\Omega) = \sum_{k=1}^{3} \mathbf{p}_k(\Omega) = \frac{p(\Omega)}{\sqrt{2}} \sum_{k=1}^{3} \left[\hat{e}_+ + e^{(k-1)\frac{2i\pi}{3}}\ \hat{e}_-\right] = \frac{3\ p(\Omega)}{\sqrt{2}}\ \hat{e}_+. \tag{17}$$

It follows from Eq. (17) that the net left-handed polarization $\mu_{\mathrm{THz}} = +1$ results from the constructive interference of the left-handed components $\hat{e}_+$ of the dipoles carried by the individual nanoribbons. The right-handed components $\hat{e}_-$ interfere destructively.

Since the nonlinear dipole $\mathbf{p}_k(\Omega)$ induced in each individual centrosymmetric nanoribbon stems from the near-field interactions, re-positioning a nanoribbon by the δx and δy displacements (see Fig.4b and Fig.4c) lifts the absolute value degeneracy of the $\mathbf{p}_{k=1,2,3}(\Omega)$ dipoles (but do not change the orientation of the dipoles). This, in turn, affects the interference of different contributions when computing the total dipole and thus $\mathcal{I}_p(\Omega)$. Similarly, changing the length L of one of the GNRs (Fig.4e) shifts its plasmon resonance and thus modifies its (i) linear and (ii) nonlinear response, affecting the phases and amplitudes of the induced dipoles $\mathbf{p}_{k=1,2,3}(\Omega)$ and hence their interference. Rotation of one of the nanoribbons (changing angle φ_k) primarily affects the relative phase of the corresponding nonlinear dipole. It thus degrades the destructive interference for $\hat{e}_-$ components of the DFG in Eq. (17), and strongly affects the polarization index $\mathcal{I}_p(\Omega)$ of the emitted THz radiation. The analytical expression for the nonlinear response of the C3 compound given by Eq. (17) helps thus to understand numerical results reported in Fig.4.

Breaking centrosymmetry of the nanoribbons

In this subsection, we show that breaking the centrosymmetric character of the GNRs is lifting the effect of geometry distortions caused by the nanoribbon δx and δy displacements. Consider first the C3 compound of non-centrosymmetric identical nanoribbons and contra-rotating continuous wave (cw) fields $\mathbf{E}_1(t)$ and $\mathbf{E}_2(t)$ given by Eq. (6) with $E_0(t) = A_0$. In this situation, the longitudinal nonlinear dipole $\mathbf{p}_k^{cw}(\Omega)$ induced in each nanoribbon can be expressed as

$$\mathbf{p}_k^{cw}(\Omega) = A_0^2 \, \left(\alpha_L^{(2)}(\Omega) + \mathcal{C}_k(\Omega)\right) \, \exp(-i2\varphi_k) \, \hat{e}_k, \tag{18}$$

where φ_k and $\hat{e}_k$ are defined in the previous subsection. The first term in brackets accounts for the nonlinear dipole owing to the incident fields with $\alpha_L^{(2)}(\Omega)$ being the longitudinal second-order hyperpolarizability. The second term in brackets accounts for the effect of the induced fields created by the neighbouring GNRs.

Consider now that the separations between the nanoribbons are such that $\mathcal{C}_k(\Omega) \ll \alpha_L^{(2)}$. For the present system, this corresponds to separations between the closest extremities of the nanoribbons greater than 25 nm, as verified by TDDF-TB calculations (see Fig. 5). In the absence of inter-ribbon interactions Eq. 18 transforms to

$$\mathbf{p}_k^{cw}(\Omega) = A_0^2 \, \alpha_L^{(2)}(\Omega) \, \exp(-i2\varphi_k) \, \hat{e}_k. \tag{19}$$

Adopting a general interpretation not constrained by the C3 symmetry, where $\hat{e}_k$ is the unit-length vector along a GNR oriented at an angle φ_k with respect to the x-axis, one recognizes that Eq. (19) provides the nonlinear dipole induced in the individual free-standing GNR. As follows from Eq. (17), the selectivity of the polarization states of the DFG is ensured by the interference between the nonlinear dipoles induced in the three nanoribbons. To this end, (i) the amplitudes of the dipoles must be the same, and (ii) their relative phases $\varphi_{k+1} - \varphi_k$ must differ by $2\pi/3$. With $\mathbf{p}_k^{cw}(\Omega)$ given by Eq. (19), the first and second conditions do not depend on geometry variations given by the δx and δy displacements of the nanoribbons along x and y directions.

This is an important result: for identical noninteracting, non-centrosymmetric nanoribbons oriented such that $\varphi_{k+1} - \varphi_k = 2\pi/3$, Eq. (17) holds and the DFG with $\mu_{\mathrm{THz}} = +1$ is robust *irrespective of the positions* of the nanoribbons in the 2D (x, y)-plane. As an example, their extremities can be aligned, which means that the global shape of the compound is very far from C3 symmetry, although its behavior with respect to THz generation is strictly that

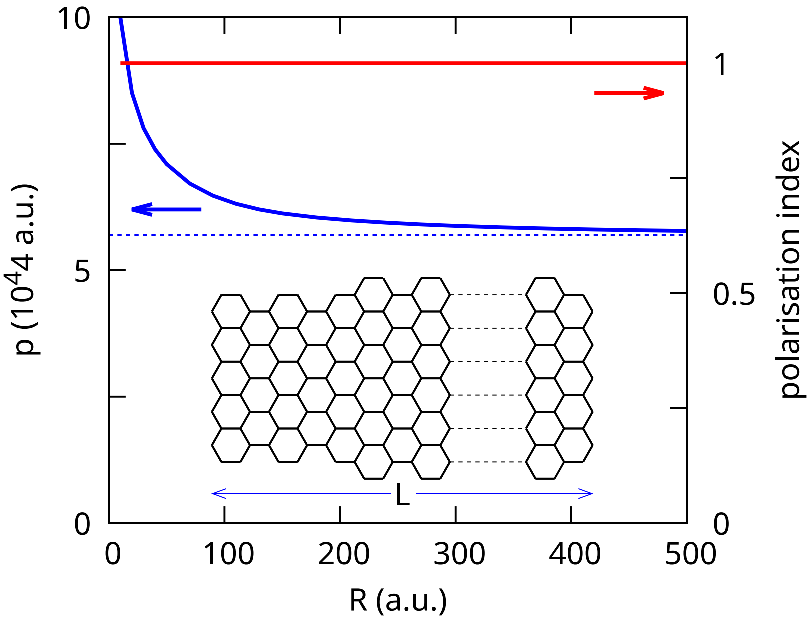

Figure 5: TDDM-TB results for the DFG generation from an ideal C3 compound of identical non-centrosymmetric GNRs. The nonlinear response is induced by two contra-rotating circularly polarized electromagnetic pulses one with $\omega_1 = 177$ meV and $\mu_1 = -1$, and the other one with $\omega_2 = 147$ meV and $\mu_2 = +1$. The geometry of an individual nanoribbon with $L = 396$ a.u. is sketched in the insert. The geometry of the compound system is sketched in Fig. 2a. The narrowest end of GNRs is pointing towards the center of the compound. The amplitude $|\mathbf{p}(\Omega)|$ (blue line, left vertical axis), and polarization index $\mathcal{I}_p(\Omega)$ (red line, right vertical axis) of the induced nonlinear dipole at the difference frequency $\Omega = 30$ meV are shown as a function of the geometry parameter R. The dotted blue line indicates the asymptotic value of $|\mathbf{p}(\Omega)|$.

of a C3 compound. Thus, Neumann's principle determines a sufficient, but not necessary, condition to ensure the selectivity of the polarization state of the field radiated at the difference frequency. It is also worth noting that such a compound structure should feature a nonlinear circularly polarized THz dipole independent of the location of the nanoribbons with respect to each other

$$p_+^{cw}(\Omega) = \frac{3}{\sqrt{2}} A_0^2 \alpha_L^{(2)}(\Omega), \tag{20}$$

as can be obtained from Eq. (17) replacing $p(\Omega)$ by $A_0^2\ \alpha_L^{(2)}(\Omega)$ (see Eq. (19)).

This said, while robust against GNRs translation in the (x, y)-plane, the interference conditions remain sensitive to the variations of the orientation of the GNRs and to the variations of their length δL. The latter is mainly related to the shift of their dipolar plasmon resonance frequency leading to different hyperpolarizabilities $\alpha_L^{(2)}(\Omega)$, and thus to different amplitudes of the dipoles induced by the DFG.

To test the effect of the centrosymmetry break of GNRs we transformed an ideal aGNR13 nanoribbons into non-centrosymmetric ones by removing 8 carbon atoms at one of their ends (see the sketch of the non-centrosymmetric GNR in the insert of Fig. 5). The length $L = 396$ a.u. of the original GNRs and their electrostatic doping by 6 electrons is preserved. The change in geometry results in a 5 meV redshift of the dipolar plasmon frequency of the individual non-centrosymmetric nanoribbon.

For the sake of comparison with the compound of aGNR13 nanoribbons (Fig. 3), we show in Fig. 5 the DFG from an ideal C3 symmetry compound of identical non-centrosymmetric GNRs. The TDDM-TB calculations are performed for different values of the geometry parameter R. The nonlinear effect is induced by two contra-rotating circularly polarized electromagnetic pulses one with $\omega_1 = 177$ meV and the other one with $\mu_1 = -1$, and $\omega_2 = 147$ meV and $\mu_2 = +1$. The incident electromagnetic radiation is thus the same as in the subsection above devoted to centrosymmetric aGNR13 nanoribbons, except that ω_1 and ω_2 have been redshifted by 5 meV to account for the corresponding redshift of the $\omega_{\rm DP}$. The geometry of the compound is sketched in Fig. 2a, where the narrowest end of the nanoribbon is pointing towards the center of the compound. The main difference when comparing results in Fig. 3 and in Fig. 5 appears at large separations R, where the mutual interactions between nanoribbons tend to zero. As discussed above, for the compound of centrosymmetric aGNR13 nanoribbons the induced nonlinear dipole vanishes in this situation (see Fig. 3). In contrast, for the compound of the non-centrosymmetric GNRs the amplitude of the induced nonlinear dipole $|\mathbf{p}(\Omega)|$ tends to the asymptotic limit approximately given by Eq. (20). The "approximately" is used here because Eq. (20) is derived for the cw fundamental field, while in TDDM-TB calculations we consider fundamental pulses of finite duration.

In Fig. 6, we study the consequences of the geometry distortions linked with misalignment

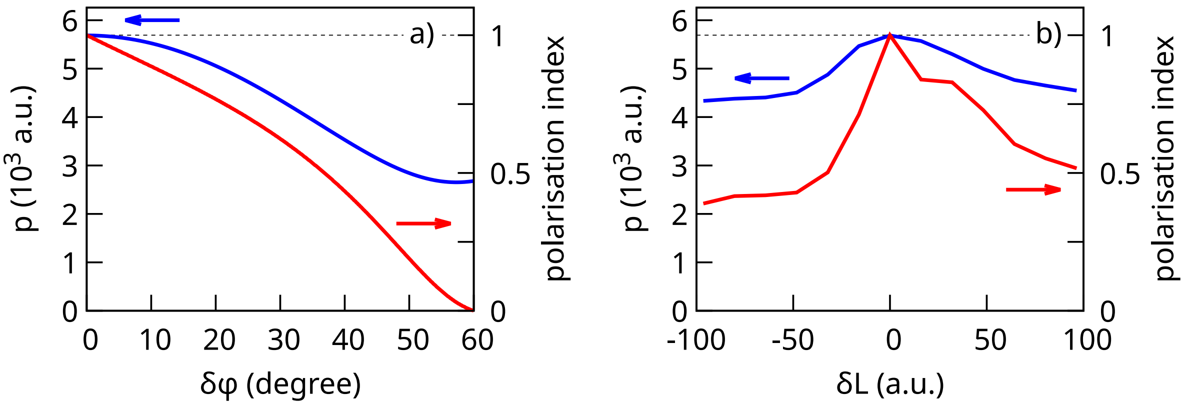

Figure 6: Effect of the geometry distortion on the DFG from the compound of three noninteracting, non-centrosymmetric GNRs (an individual nanoribbon is sketched in Fig. 5). The nonlinear response is induced by two contra-rotating circularly polarized electromagnetic pulses one with $\omega_1 = 177$ meV and $\mu_1 = -1$, and the other one with $\omega_2 = 147$ meV and $\mu_2 = +1$. The amplitude $|\mathbf{p}(\Omega)|$ (blue line, left vertical axis), and polarization index $\mathcal{I}_p(\Omega)$ (red line, right vertical axis) of the induced nonlinear dipole at the difference frequency $\Omega = 30$ meV are shown as a function of the geometry distortion parameters $\delta\varphi$ and δL. Parameter $\delta\varphi$ describes the rotation of one of the GNRs from an ideal orientation given by the angle $\varphi_k = 2\pi(k-1)/3$ ($k = 1, 2, 3$) with respect to x-axis, and δL describes elongation of one of the GNRs with respect to its nominal length $L = 396$ a.u.. **Panel a:** The nanoribbon is rotated by $\delta\varphi$ while $\delta L = 0$. **Panel b:** The length of the nanoribbon is changed to $L + \delta L$ while $\delta\varphi = 0$.

of the non-centrosymmetric nanoribbons and variation of their length. We consider the compound of three noninteracting GNRs. The incident fields are the same as those used to obtain results for the C3 compound in Fig. 5. The nonlinear response of the compound structure is determined as follows. First, the nonlinear THz dipole $\mathbf{p}_k(\Omega)$ is calculated using TDDM-TB for each GNR independently. Second, the total dipole of the compound is obtained as the vector sum of the individual contributions $\mathbf{p}_{\text{comp}}(\Omega) = \sum_{k=1}^{3} \mathbf{p}_k(\Omega)$. As discussed above, breaking the centrosymmetry of GNRs allows the robust generation of the circularly polarized nonlinear dipole $\mathbf{p}_{\text{comp}}$ at THz frequency irrespective of the location of the nanoribbons. It is not sensitive to the translations of the nanoribbons along x and y axes. At the same time, it follows from the TDDM-TB results that the compound structure of non-centrosymmetric GNRs remains as sensitive to the variation of the orientation and of the length of the nanoribbons as the one made of centrosymmetric nanoribbons (compare

Fig. 6a and Fig.6 with Fig. 4c and Fig. 4d). Indeed, variation of the nanoribbon length δL and orientation $\delta\varphi_k$ changes the interference effects between the nonlinear dipoles in Eq. (17) and affects the SAM selectivity of the DFG process.

Retrieval of the SAM selectivity of the THz generation for a large set of nanoribbon compounds

It follows from the results in previous sections that the SAM selection rules for the circular polarization states of DFG by individual graphene nanostructures are significantly altered by the atomic-scale defects and macroscopic geometry variations. Nonetheless, for harmonic frequency generation with graphene nanoflakes we have found,[68] that averaging over a large ensemble of the nanostructures, such as metasurface, can substantially reduce the effect of the imperfections. The behavior of an ideal system could be partially restored. This finding explains why the symmetry selection rules for the circularly polarized harmonics have been observed with plasmonic metamaterials,[52,56,57] even though each individual meta-atom obviously does not possess an ideal symmetry.

Indeed, consider the C3 compound system of aGNR13 nanoribbons as discussed in Fig. 2, Fig. 3, and Fig. 4. Assuming a small geometry variation from an ideal Eq. (17) transforms to:

$$\mathbf{p}_{\mathrm{comp}}(\Omega) \approx \frac{p(\Omega)}{\sqrt{2}}\left[3(1+\kappa_+)\ \hat{e}_+\ +\kappa_-\ \hat{e}_-\right] \tag{21}$$

where $\kappa_\pm$ are complex-valued numbers with $|\kappa_\pm| \ll 1$. Random defects lead to a random distribution of $\kappa_\pm$. Eventually, its expectation value might be close to zero allowing retrieval of an ideal system.

To examine if it is the case, we studied the polarization states of the DFG induced in a large set of randomly distorted C3 (we label compounds according to their symmetry in an ideal case) compounds of aGNR13 nanoribbons arranged on a 2D surface. To keep the calculation tractable, we considered that there is no interaction between compounds, while the aGNR13 nanoribbons within each compound interact. In this situation, the DFG by the ensemble of aGNR13 compounds can be obtained from the vector sum of the nonlinear dipoles at difference frequency Ω calculated using the TDDM-TB method separately for each individual aGNR13 compound. Since the calculation time for TDDM-TB scales as the cube of the number of carbon atoms treated simultaneously, this approach results in a significant reduction in computational effort. We have shown (see SI) that for distances between compounds $\gtrsim 3000$ a.u. ($\gtrsim 150$ nm) the noninteracting approximation holds, provided that collective effects linked to lattice resonances[103–105] can be neglected. Given the frequencies of the contra-rotating circularly polarized electromagnetic pulses incident on the system ($\omega_1 = 182$ meV, and $\omega_2 = 152$ meV), one can arrange approximately 10^3 independent aGNR13 compounds in a circle with a diameter substantially smaller than the wavelengths $\lambda \sim 7.4 \times 10^3$ nm of the incident fields. A large 2D set of GNR compounds, with an average distance between them ($\gtrsim 150$ nm) can thus be regarded as a portion of a metasurface.

Starting with a perfect C3 arrangement of the $L = 396$ a.u. aGNR13 nanoribbons characterized by $R = 100$ a.u. (see Fig. 2), we generated a sample of 512 randomly deformed nanostructures. Using TDDM-TB, we computed the nonlinear THz dipole $\mathbf{p}_{\mathrm{comp,j}}(\Omega)$ ($1 \leq j \leq 512$) induced in each of them independently. Finally, the total induced THz dipole of the random 2D array containing $\mathcal{N}$ compounds ($\mathcal{N} = 1, 2, 4, 8, \ldots, 128$), is given by

$$\mathbf{p}_{\mathcal{N}}(\Omega) = \sum_{j=j_1,\ldots,j_{\mathcal{N}}} \mathbf{p}_{\mathrm{comp,j}}(\Omega), \tag{22}$$

For each value of $\mathcal{N}$, the simulation is repeated for $512/\mathcal{N}$ independent samples of $j_1, \ldots, j_{\mathcal{N}}$ compounds, enabling us to estimate the statistical dispersion of the results.

The geometries of the deformed nanostructures were generated using the following approach. First, the length of each of the three nanoribbons was modified independently by randomly chosen δL while keeping the center position and orientation of the nanoribbon constant. The random choice of δL follows a normal distribution centered on zero with a

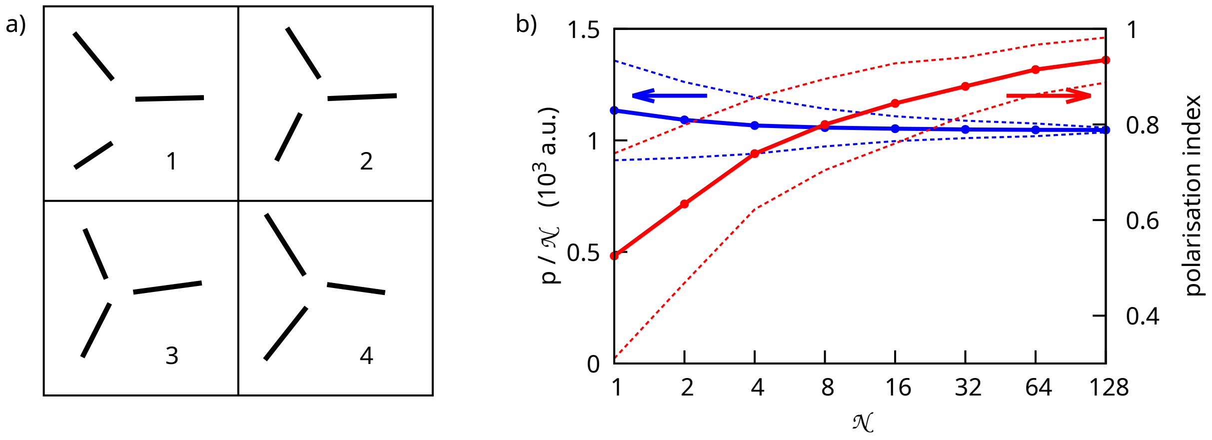

Figure 7: DFG from a 2D array of $\mathcal{N}$ distorted aGNR13 compounds. An ideal C3 compound comprises GNRs with a length of $L = 396$ a.u.. The geometry parameter $R = 100$ a.u. (see Fig. 2 for the geometry). The nonlinear response is induced by two contra-rotating circularly polarized electromagnetic pulses one with $\omega_1 = 182$ meV and $\mu_1 = -1$, and the other one with $\omega_2 = 152$ meV and $\mu_2 = +1$. **Panel a:** an example of four distorted compounds. **Panel b:** the amplitude $|\mathbf{p}(\Omega)|$ per compound (blue lines, left vertical axis) and the polarization index $\mathcal{I}_p(\Omega)$ (red lines, right vertical axis) of the total nonlinear THz dipole of the array. The dipole $\mathbf{p}(\Omega)$ at the difference frequency $\Omega = \omega_1 - \omega_2 = 30$ meV is obtained by statistical average over randomly composed 2D arrays of $\mathcal{N}$ distorted aGNR13 compounds. For further details, see the main text of the paper. Results are shown as a function of $\mathcal{N}$. The solid lines are the mean values, while the dashed lines indicate the mean values plus or minus standard deviation.

standard deviation of 37.8 a.u. (2 nm). The value of δL is then adjusted to the closest value that preserves the shape of the nanoribbon at its ends. Second, the coordinates x and y of the two ends of each of the three nanoribbons are randomly shifted, slightly changing their orientation. Each of these shifts follows a normal distribution centered on zero with a standard deviation of 18.7 a.u. (1 nm), subject to the constraint of respecting the length L as fixed in the first step. Fig. 7a provides an example of a four aGNR13 compound geometries produced using this method.

The calculated statistical improvement in the polarization state of the DFG from the disordered 2D array of $\mathcal{N}$ nanostructures with geometry distortions is shown in detail in Fig. 7b. It follows from our results that using a relatively small number of compounds enables one to largely mitigate the effect of the non-ideal C3 symmetry of each nanostructure and to significantly enhance the handedness of the induced THz dipole. In fact, the effect of the average of the geometry fluctuations is already visible for a small set of only four compounds $\mathcal{N} = 4$ as shown in Fig. 7a. For example, individually aGNR13 compounds labelled with 1,2,3, and 4 generate THz dipoles characterized by the polarisation index 0.6 (compound 1), 0.27 (compound 2), 0.24 (compound 3), and 0.60 (compound 4). This is while collectively they generate a THz dipole with a higher polarization index of 0.72 (and an amplitude approximately 4× the mean amplitude), i.e., closer to an ideal structure. It is worth noting that for $\mathcal{N} \to 128$ the absolute value of the nonlinear dipole induced per distorted aGNR13 compound tends, with very small dispersion, to a constant value, which is only 10% lower than that for an ideal C3 compound nanostructure. We have made the pinpoint tests showing that the statistical average allows for retrieval of the polarization selectivity of DFG also for defective triangular nanoflakes (see SI).

All in all findings presented in this subsection provide evidence that the theoretical results obtained for ideal nanostructures can also be exploited in realistic situations involving unavoidable structural and geometrical symmetry distortions.

As a final remark, considering the metasurface built from noninteracting graphene nanostructures (triangular nanoflakes or GNR compounds) allows us to compare its DFG performance with earlier findings for mode-matching metamaterials[106] (infra-red DFG) or nonlinear metasurfaces loaded with multi-quantum-well structures[59] (THz DFG). To this end we define two parameters: (i) the DFG conversion efficiency per area of the unit cell $\mathcal{S}$ as $\eta = P_\Omega(P_{\omega_1} P_{\omega_2})^{-1}$, where P_ω stands for the intensity of electromagnetic field at frequency ω; and (ii) the metasurface conversion efficiency as $\eta_{\mathrm{MS}} = P_\Omega(P_{\omega_1} + P_{\omega_2})^{-1}$. As we show in SI, using systems addressed here as noninteracting meta-atoms, and considering a surface unit cell area $\mathcal{S} = 150 \times 150$ nm^2, we obtain $\eta = 2 \times 10^{-4} - 1 \times 10^{-2}$ W/W^2. This performance is comparable to that reported for the mode-matching metamaterials.[106] We further find that $\eta_{\mathrm{MS}} = 2 \times 10^{-9}\ \% - 1 \times 10^{-7}\ \%$ for $I_{\mathrm{pump}} = 1$ kW/cm^2. While this is four orders of magnitude lower than the conversion efficiencies reported for nonlinear metasurfaces loaded with multi-quantum-well structures,[59] it is important to note that the packing density of triangular nanoflakes is 1.2 %, and 0.4 % for nanoribbon compounds. Given that η_{MS} scales with the square of the surface area, the performance per nonlinear element (or meta-atom) remains comparable to that in the work of Tymchenko *et al*,[59] where the packing density of the metasurfaces loaded with multi-quantum-well structures is close to 40 %. We emphasize that Refs.[59,106] report *linearly polarized DFG*, while we address the SAM selective generation of *circularly polarized DFG* in the THz frequency range. Our findings thus reaffirm the potential of graphene as a platform for nonlinear applications.

Summary, conclusions and outlook

Using the time-dependent density matrix technique based on the tight-binding description of the π-electrons in graphene we studied theoretically the nonlinear DFG from graphene nanostructures enabling THz generation in the far field. Such nanostructures can be seen as meta-atoms for nonlinear metasurfaces. Along with numerical analysis, the Neumann's symmetry principle has been applied for the analytical derivation of the polarization states of the nonlinear dipole induced in graphene at the difference frequency. According to the analytical theory, circularly polarized THz radiation with controllable SAM (handedness) can be obtained in the far-field emission perpendicular to the graphene surface. To this end, an individual nanoflake or a compound system of several nanoflakes with C3 symmetry has to be subjected to two electromagnetic fields (i) circularly polarized in the graphene plane and (ii) of opposite handedness. The numerical simulations fully confirm the selective generation of THz radiation with controllable SAM under relevant conditions.

First, we considered ideal situations of perfect C3 symmetry systems such as triangular graphene nanoflakes or compound structures made of GNRs. To enhance the nonlinear response, the incident electromagnetic fields are in near resonance with the dipolar plasmon of graphene nanostructure.

Second, we addressed a perspective of the practical implementations and we found that the unavoidable atomic-scale defects of the nanoflakes strongly affect the polarization states of the DFG, leading to the loss of the possibility to control the SAM of the THz radiation. In this respect, bottom-up approaches available nowadays can be used to built small aGNR13 graphene nanoribbons without atomic-scale defects. However, macroscopic geometry distortions are unavoidable when arranging nanoribbons into a C3 compound structure. It follows from our results that such distortions also strongly degrade the performance of the device.

Finally, we studied strategies to improve the SAM selectivity of circular THz radiation produced by DFG in graphene nanostructures despite imperfections associated with their fabrication. We have shown that functionalization of the nanoribbons that breaks their centrosymmetry allows reducing the effect of geometric distortion in a compound nanostructure built from such nanoribbons. However, the most promising approach demonstrated here for noninteracting defective C3 nanostructures consists in statistical averaging over their large set, as would be the case for, e.g., metasurface. We obtained that random deviations breaking C3 symmetry of each individual nanostructure tend to average to zero, allowing retrieval of the polarization state and efficiency close to that of an ideal device.

We believe that being at the interface of the two active fields of research, namely (i) manipulation and generation of THz radiation with 2D materials including graphene and (ii) utilizing nonlinear metasurfaces for manipulating structured light, our results contribute to the analysis of challenges and opportunities in utilizing the strong nonlinear response of graphene. Importantly, beyond the DFG of THz radiation considered in this work, or high harmonic generation described earlier,[68] the statistical retrieval of nonlinear polarization states reported here should be generally applicable to the use of graphene nanostructures as SAM-controllable frequency mixers.[18,107,108]

Supporting Information Available

The following files are available free of charge. Supporting Information providing

- The TDDM-TB method;
- Selection rules for nonlinear multipole moments induced by circularly polarized light;
- Effect of the number of carbon atom vacancies on the dipolar plasmonic resonance;
- Third harmonic generation from armchair graphene nanoribbons;
- Limits of the perturbative regime of nonlinear response;
- Effect of the choice relaxation parameter γ;
- Range of the interaction between C3 compounds of aGNR13 nanoribbons;
- Statistical improvement of the circular polarization control for the THz generation from triangular nanoflakes;
- Estimate of the DFG efficiency for graphene nanostructures arranged in metasurface, comparison with earlier findings.

References

(1) Valušis, G.; Lisauskas, A.; Yuan, H.; Knap, W.; Roskos, H. G. Roadmap of Terahertz Imaging 2021. *Sensors* **2021**, *21*.

(2) Naftaly, M.; Vieweg, N.; Deninger, A. Industrial Applications of Terahertz Sensing: State of Play. *Sensors* **2019**, *19*.

(3) Chan, W. L.; Deibel, J.; Mittleman, D. M. Imaging with terahertz radiation. *Reports on Progress in Physics* **2007**, *70*, 1325.

(4) Jepsen, P.; Cooke, D.; Koch, M. Terahertz spectroscopy and imaging – Modern techniques and applications. *Laser & Photonics Reviews* **2011**, *5*, 124–166.

(5) Tonouchi, M. Cutting-edge terahertz technology. *Nature Photonics* **2007**, *1*, 97–105.

(6) Leitenstorfer, A.; Moskalenko, A. S.; Kampfrath, T.; Kono, J.; Castro-Camus, E.; Peng, K.; Qureshi, N.; Turchinovich, D.; Tanaka, K.; Markelz, A. G. et al. The 2023 terahertz science and technology roadmap. *Journal of Physics D: Applied Physics* **2023**, *56*, 223001.

(7) Bitzer, A.; Merbold, H.; Thoman, A.; Feurer, T.; Helm, H.; Walther, M. Terahertz near-field imaging of electric and magnetic resonances of a planar metamaterial. *Opt. Express* **2009**, *17*, 3826–3834.

(8) Hillenbrand, R.; Abate, Y.; Liu, M.; Chen, X.; Basov, D. N. Visible-to-THz near-field nanoscopy. *Nature Reviews Materials* **2025**, *10*, 285–310.

(9) Cocker, T. L.; Jelic, V.; Gupta, M.; Molesky, S. J.; Burgess, J. A. J.; Reyes, G. D. L.; Titova, L. V.; Tsui, Y. Y.; Freeman, M. R.; Hegmann, F. A. An ultrafast terahertz scanning tunnelling microscope. *Nature Photonics* **2013**, *7*, 620–625.

(10) Yoshioka, K.; Katayama, I.; Arashida, Y.; Ban, A.; Kawada, Y.; Konishi, K.; Takahashi, H.; Takeda, J. Tailoring Single-Cycle Near Field in a Tunnel Junction with Carrier-Envelope Phase-Controlled Terahertz Electric Fields. *Nano Letters* **2018**, *18*, 5198–5204.

(11) Kang, T.; Bahk, Y.-M.; Kim, D.-S. Terahertz quantum plasmonics at nanoscales and angstrom scales. *Nanophotonics* **2020**, *9*, 435–451.

(12) Cocker, T. L.; Jelic, V.; Hillenbrand, R.; Hegmann, F. A. Nanoscale terahertz scanning probe microscopy. *Nature Photonics* **2021**, *15*, 558–569.

(13) Kimura, K.; Morinaga, Y.; Imada, H.; Katayama, I.; Asakawa, K.; Yoshioka, K.; Kim, Y.; Takeda, J. Terahertz-field-driven scanning tunneling luminescence spectroscopy. *ACS Photonics* **2021**, *8*, 982–987.

(14) Müller, M. Imaging surfaces at the space–time limit: New perspectives of time-resolved scanning tunneling microscopy for ultrafast surface science. *Progress in Surface Science* **2024**, *99*, 100727.

(15) Jelic, V.; Adams, S.; Hassan, M.; Cleland-Host, K.; Ammerman, S. E.; Cocker, T. L. Atomic-scale terahertz time-domain spectroscopy. *Nature Photonics* **2024**, *18*, 898–904.

(16) Siday, T.; Hayes, J.; Schiegl, F.; Sandner, F.; Menden, P.; Bergbauer, V.; Zizlsperger, M.; Nerreter, S.; Lingl, S.; Repp, J. et al. All-optical subcycle microscopy on atomic length scales. *Nature* **2024**, *629*, 329–334.

(17) Wimmer, L.; Herink, G.; Solli, D. R.; Yalunin, S. V.; Echternkamp, K. E.; Ropers, C. Terahertz control of nanotip photoemission. *Nature Physics* **2014**, *10*, 432.

(18) Autere, A.; Jussila, H.; Dai, Y.; Wang, Y.; Lipsanen, H.; Sun, Z. Nonlinear Optics with 2D Layered Materials. *Advanced Materials* **2018**, *30*, 1705963.

(19) Shi, J.; Li, Z.; Sang, D. K.; Xiang, Y.; Li, J.; Zhang, S.; Zhang, H. THz photonics in two dimensional materials and metamaterials: properties, devices and prospects. *J. Mater. Chem. C* **2018**, *6*, 1291–1306.

(20) Mittendorff, M.; Winnerl, S.; Murphy, T. E. 2D THz Optoelectronics. *Advanced Optical Materials* **2021**, *9*, 2001500.

(21) Vitiello, M. S.; Viti, L. Engineering THz-frequency light generation, detection, and manipulation through graphene. *Applied Physics Reviews* **2025**, *12*, 011321.

(22) Zhang, J.; Zhao, W.; Yu, P.; Yang, G.; Liu, Z. Second harmonic generation in 2D layered materials. *2D Materials* **2020**, *7*, 042002.

(23) Mikhailov, S. A. Theory of the giant plasmon-enhanced second-harmonic generation in graphene and semiconductor two-dimensional electron systems. *Phys. Rev. B* **2011**, *84*, 045432.

(24) Cox, J. D.; García de Abajo, F. J. Nonlinear Graphene Nanoplasmonics. *Accounts of Chemical Research* **2019**, *52*, 2536–2547.

(25) Cox, J. D.; Marini, A.; García de Abajo, F. J. Plasmon-assisted high-harmonic generation in graphene. *Nature Communications* **2017**, *8*, 14380.

(26) Cox, J. D.; García de Abajo, F. J. Plasmon-Enhanced Nonlinear Wave Mixing in Nanostructured Graphene. *ACS Photonics* **2015**, *2*, 306–312.

(27) Glazov, M.; Ganichev, S. High frequency electric field induced nonlinear effects in graphene. *Physics Reports* **2014**, *535*, 101–138.

(28) Ullah, K.; Meng, Y.; Shi, Y.; Wang, F. Harmonic generation in low-dimensional materials. *Advanced Optical Materials* **2022**, *10*, 2101860.

(29) Manzoni, M. T.; Silveiro, I.; de Abajo, F. J. G.; Chang, D. E. Second-order quantum nonlinear optical processes in single graphene nanostructures and arrays. *New Journal of Physics* **2015**, *17*, 083031.

(30) Soavi, G.; Wang, G.; Rostami, H.; Purdie, D. G.; De Fazio, D.; Ma, T.; Luo, B.; Wang, J.; Ott, A. K.; Yoon, D. et al. Broadband, electrically tunable third-harmonic generation in graphene. *Nature Nanotechnology* **2018**, *13*, 583–588.

(31) Brun, S. J.; Pedersen, T. G. Intense and tunable second-harmonic generation in biased bilayer graphene. *Phys. Rev. B* **2015**, *91*, 205405.

(32) Zhang, Y.; Huang, D.; Shan, Y.; Jiang, T.; Zhang, Z.; Liu, K.; Shi, L.; Cheng, J.; Sipe, J. E.; Liu, W.-T. et al. Doping-induced second-harmonic generation in centrosymmetric graphene from quadrupole response. *Phys. Rev. Lett.* **2019**, *122*, 047401.

(33) An, Y. Q.; Nelson, F.; Lee, J. U.; Diebold, A. C. Enhanced optical second-harmonic generation from the current-biased graphene/SiO2/Si(001) structure. *Nano Letters* **2013**, *13*, 2104–2109.

(34) Yoshikawa, N.; Tamaya, T.; Tanaka, K. High-harmonic generation in graphene enhanced by elliptically polarized light excitation. *Science* **2017**, *356*, 736–738.

(35) Jablan, M.; Buljan, H.; Soljačić, M. Plasmonics in graphene at infrared frequencies. *Phys. Rev. B* **2009**, *80*, 245435.

(36) Castro Neto, A. H.; Guinea, F.; Peres, N. M. R.; Novoselov, K. S.; Geim, A. K. The electronic properties of graphene. *Rev. Mod. Phys.* **2009**, *81*, 109–162.

(37) Grigorenko, A. N.; Polini, M.; Novoselov, K. S. Graphene plasmonics. *Nature Photonics* **2012**, *6*, 749–758.

(38) García de Abajo, F. J. Graphene plasmonics: challenges and opportunities. *ACS Photonics* **2014**, *1*, 135–152.

(39) Maysonnave, J.; Huppert, S.; Wang, F.; Maero, S.; Berger, C.; de Heer, W.; Norris, T. B.; De Vaulchier, L. A.; Dhillon, S.; Tignon, J. et al. Terahertz Generation by Dynamical Photon Drag Effect in Graphene Excited by Femtosecond Optical Pulses. *Nano Letters* **2014**, *14*, 5797–5802.

(40) Bahk, Y.-M.; Ramakrishnan, G.; Choi, J.; Song, H.; Choi, G.; Kim, Y. H.; Ahn, K. J.; Kim, D.-S.; Planken, P. C. M. Plasmon Enhanced Terahertz Emission from Single Layer Graphene. *ACS Nano* **2014**, *8*, 9089–9096.

(41) Prechtel, L.; Song, L.; Schuh, D.; Ajayan, P.; Wegscheider, W.; Holleitner, A. W. Time-resolved ultrafast photocurrents and terahertz generation in freely suspended graphene. *Nature Communications* **2012**, *3*, 646.

(42) Zhang, D.; Xu, Z.; Cheng, G.; Liu, Z.; Gutierrez, A. R.; Zang, W.; Norris, T. B.; Zhong, Z. Strongly enhanced THz generation enabled by a graphene hot-carrier fast lane. *Nature Communications* **2022**, *13*, 6404.

(43) Constant, T. J.; Hornett, S. M.; Chang, D. E.; Hendry, E. All-optical generation of surface plasmons in graphene. *Nature Physics* **2016**, *12*, 124–127.

(44) Yao, B.; Liu, Y.; Huang, S.-W.; Choi, C.; Xie, Z.; Flor Flores, J.; Wu, Y.; Yu, M.; Kwong, D.-L.; Huang, Y. et al. Broadband gate-tunable terahertz plasmons in graphene heterostructures. *Nature Photonics* **2018**, *12*, 22–28.

(45) Yao, X.; Tokman, M.; Belyanin, A. Efficient Nonlinear Generation of THz Plasmons in Graphene and Topological Insulators. *Phys. Rev. Lett.* **2014**, *112*, 055501.

(46) Keren-Zur, S.; Avayu, O.; Michaeli, L.; Ellenbogen, T. Nonlinear Beam Shaping with Plasmonic Metasurfaces. *ACS Photonics* **2016**, *3*, 117–123.

(47) Chen, S.; Li, K.; Deng, J.; Li, G.; Zhang, S. High-Order Nonlinear Spin–Orbit Interaction on Plasmonic Metasurfaces. *Nano Letters* **2020**, *20*, 8549–8555.

(48) Buono, W. T.; Forbes, A. Nonlinear optics with structured light. *Opto-Electronic Advances* **2022**, *5*, 210174–1–210174–19.

(49) Koenderink, A. F.; Alù, A.; Polman, A. Nanophotonics: Shrinking light-based technology. *Science* **2015**, *348*, 516–521.

(50) Krasnok, A.; Tymchenko, M.; Alù, A. Nonlinear metasurfaces: a paradigm shift in nonlinear optics. *Materials Today* **2018**, *21*, 8–21.

(51) Li, G.; Sartorello, G.; Chen, S.; Nicholls, L. H.; Li, K. F.; Zentgraf, T.; Zhang, S.; Zayats, A. V. Spin and Geometric Phase Control Four-Wave Mixing from Metasurfaces. *Laser & Photonics Reviews* **2018**, *12*, 1800034.

(52) Konishi, K.; Kan, T.; Kuwata-Gonokami, M. Tunable and nonlinear metamaterials for controlling circular polarization. *Journal of Applied Physics* **2020**, *127*, 230902.

(53) Koshelev, K.; Tang, Y.; Hu, Z.; Kravchenko, I. I.; Li, G.; Kivshar, Y. Resonant Chiral Effects in Nonlinear Dielectric Metasurfaces. *ACS Photonics* **2023**, *10*, 298–306.

(54) Jangid, P.; Vincenti, M. A.; Carletti, L.; Rudenko, A.; Kivshar, Y.; Kruk, S. Chiral High-Harmonic Generation in Metasurfaces. *ACS Photonics* **2025**, *12*, 4342–4348.

(55) Coudrat, L.; Boulliard, G.; Gérard, J.-M.; Lemaître, A.; Degiron, A.; Leo, G. Unravelling the nonlinear generation of designer vortices with dielectric metasurfaces. *Light: Science and Applications* **2025**, *14*, 51.

(56) Chen, S.; Li, G.; Zeuner, F.; Wong, W. H.; Pun, E. Y. B.; Zentgraf, T.; Cheah, K. W.; Zhang, S. Symmetry-Selective Third-Harmonic Generation from Plasmonic Metacrystals. *Phys. Rev. Lett.* **2014**, *113*, 033901.

(57) Konishi, K.; Higuchi, T.; Li, J.; Larsson, J.; Ishii, S.; Kuwata-Gonokami, M. Polarization-Controlled Circular Second-Harmonic Generation from Metal Hole Arrays with Threefold Rotational Symmetry. *Phys. Rev. Lett.* **2014**, *112*, 135502.

(58) Konishi, K.; Akai, D.; Mita, Y.; Ishida, M.; Yumoto, J.; Kuwata-Gonokami, M. Circularly polarized vacuum ultraviolet coherent light generation using a square lattice photonic crystal nanomembrane. *Optica* **2020**, *7*, 855–863.

(59) Tymchenko, M.; Gomez-Diaz, J. S.; Lee, J.; Belkin, M. A.; Alù, A. Highly-efficient THz generation using nonlinear plasmonic metasurfaces. *Journal of Optics* **2017**, *19*, 104001.

(60) Li, J.; Li, J.; Yang, Y.; Li, J.; Zhang, Y.; Wu, L.; Zhang, Z.; Yang, M.; Zheng, C.; Li, J. et al. Metal-graphene hybrid active chiral metasurfaces for dynamic terahertz wavefront modulation and near field imaging. *Carbon* **2020**, *163*, 34–42.

(61) Xu, Y.; Zhang, H.; Li, Q.; Zhang, X.; Xu, Q.; Zhang, W.; Hu, C.; Zhang, X.; Han, J.; Zhang, W. Generation of terahertz vector beams using dielectric metasurfaces via spin-decoupled phase control. *Nanophotonics* **2020**, *9*, 3393–3402.

(62) Newnham, R. E. *Properties of Materials: Anisotropy, Symmetry, Structure*; Oxford University Press, 2004.

(63) Nye, J. F. *Physical Properties of Crystals, Their Representa- tions by Tensors and Matrices*; Oxford University Press, 1985.

(64) Tang, C. L.; Rabin, H. Selection Rules for Circularly Polarized Waves in Nonlinear Optics. *Phys. Rev. B* **1971**, *3*, 4025–4034.

(65) Alon, O. E.; Averbukh, V.; Moiseyev, N. Selection Rules for the High Harmonic Generation Spectra. *Phys. Rev. Lett.* **1998**, *80*, 3743–3746.

(66) Žd'ánská, P.; Averbukh, V.; Moiseyev, N. High harmonic generation spectra of aligned benzene in circular polarized laser field. *The Journal of Chemical Physics* **2003**, *118*, 8726–8738.

(67) Alejo-Molina, A.; Hardhienata, H.; Hingerl, K. Simplified bond-hyperpolarizability model of second harmonic generation, group theory, and Neumann's principle. *J. Opt. Soc. Am. B* **2014**, *31*, 526–533.

(68) Aguillon, F.; Borisov, A. G. Nonlinear Response of Nanostructured Graphene to Circularly Polarized Light. *The Journal of Physical Chemistry C* **2024**, *128*, 16576–16587.

(69) Aguillon, F.; Borisov, A. G. Atomic-Scale Defects Might Determine the Second Harmonic Generation from Plasmonic Graphene Nanostructures. *The Journal of Physical Chemistry Letters* **2023**, *14*, 238–244.

(70) Kosik, M.; Müller, M. M.; Słowik, K.; Bryant, G.; Ayuela, A.; Rockstuhl, C.; Pelc, M. Revising quantum optical phenomena in adatoms coupled to graphene nanoantennas. *Nanophotonics* **2022**, *11*, 3281–3298.

(71) Aguillon, F.; Marinica, D. C.; Borisov, A. G. Molecule detection with graphene dimer nanoantennas. *The Journal of Physical Chemistry C* **2020**, *124*, 28210–28219.

(72) Cox, J. D.; Silveiro, I.; García de Abajo, F. J. Quantum Effects in the Nonlinear Response of Graphene Plasmons. *ACS Nano* **2016**, *10*, 1995–2003, PMID: 26718484.

(73) Thongrattanasiri, S.; Manjavacas, A.; García de Abajo, F. J. Quantum Finite-Size Effects in Graphene Plasmons. *ACS Nano* **2012**, *6*, 1766–1775.

(74) Lindblad, G. On the generators of quantum dynamical semigroups. *Communications in Mathematical Physics* **1976**, *48*, 119–130.

(75) Gorini, V.; Kossakowski, A.; Sudarshan, E. C. G. Completely positive dynamical semigroups of N-level systems. *Journal of Mathematical Physics* **1976**, *17*, 821–825.

(76) Kosloff, R. Quantum thermodynamics and open-systems modeling. *The Journal of Chemical Physics* **2019**, *150*, 204105.

(77) Leforestier, C.; Bisseling, R.; Cerjan, C.; Feit, M.; Friesner, R.; Guldberg, A.; Hammerich, A.; Jolicard, G.; Karrlein, W.; Meyer, H.-D. et al. A comparison of different propagation schemes for the time dependent Schrödinger equation. *Journal of Computational Physics* **1991**, *94*, 59–80.

(78) Cox, J. D.; de Abajo, F. J. G. Transient nonlinear plasmonics in nanostructured graphene. *Optica* **2018**, *5*, 429–433.

(79) Low, T.; Avouris, P. Graphene Plasmonics for Terahertz to Mid-Infrared Applications. *ACS Nano* **2014**, *8*, 1086–1101, PMID: 24484181.

(80) Karimi, F.; Knezevic, I. Plasmons in graphene nanoribbons. *Phys. Rev. B* **2017**, *96*, 125417.

(81) Novko, D. Dopant Induced Plasmon Decay in Graphene. *Nano Letters* **2017**, *17*, 6991–6996, PMID: 28972379.

(82) Yan, H.; Low, T.; Zhu, W.; Wu, Y.; Freitag, M.; Li, X.; Guinea, F.; Avouris, P.; Xia, F. Damping pathways of mid infrared plasmons in graphene nanostructures. *Nature Photonics* **2013**, *7*, 394–399.

(83) Lewandowski, C.; Levitov, L. Intrinsically undamped plasmon modes in narrow electron bands. *Proceedings of the National Academy of Sciences* **2019**, *116*, 20869–20874.

(84) Langer, T.; Baringhaus, J.; Pfnür, H.; Schumacher, H. W.; Tegenkamp, C. Plasmon damping below the Landau regime the role of defects in epitaxial graphene. *New Journal of Physics* **2010**, *12*, 033017.

(85) Brey, L.; Fertig, H. A. Elementary electronic excitations in graphene nanoribbons. *Phys. Rev. B* **2007**, *75*, 125434.

(86) Jackson, J. D. *Classical electrodynamics*; Wiley: New York, NY, 1975.

(87) Jadidi, M. M.; König-Otto, J. C.; Winnerl, S.; Sushkov, A. B.; Drew, H. D.; Murphy, T. E.; Mittendorff, M. Nonlinear Terahertz Absorption of Graphene Plasmons. *Nano Letters* **2016**, *16*, 2734–2738, PMID: 26978242.

(88) Das Sarma, S.; Adam, S.; Hwang, E. H.; Rossi, E. Electronic transport in two-dimensional graphene. *Rev. Mod. Phys.* **2011**, *83*, 407–470.

(89) Pereira, V. M.; Guinea, F.; Lopes dos Santos, J. M. B.; Peres, N. M. R.; Castro Neto, A. H. Disorder Induced Localized States in Graphene. *Phys. Rev. Lett.* **2006**, *96*, 036801.

(90) Yuan, S.; De Raedt, H.; Katsnelson, M. I. Modeling electronic structure and transport properties of graphene with resonant scattering centers. *Phys. Rev. B* **2010**, *82*, 115448.

(91) Pereira, V. M.; Lopes dos Santos, J. M. B.; Castro Neto, A. H. Modeling disorder in graphene. *Phys. Rev. B* **2008**, *77*, 115109.

(92) Banhart, F.; Kotakoski, J.; Krasheninnikov, A. V. Structural Defects in Graphene. *ACS Nano* **2011**, *5*, 26–41, PMID: 21090760.

(93) Zobelli, A.; Ivanovskaya, V.; Wagner, P.; Suarez-Martinez, I.; Yaya, A.; Ewels, C. P. A comparative study of density functional and density functional tight binding calculations of defects in graphene. *physica status solidi (b)* **2012**, *249*, 276–282.

(94) Kotakoski, J.; Meyer, J. C.; Kurasch, S.; Santos-Cottin, D.; Kaiser, U.; Krasheninnikov, A. V. Stone-Wales-type transformations in carbon nanostructures driven by electron irradiation. *Phys. Rev. B* **2011**, *83*, 245420.

(95) Bhatt, M. D.; Kim, H.; Kim, G. Various defects in graphene: a review. *RSC Adv.* **2022**, *12*, 21520–21547.

(96) Yuan, S.; Roldán, R.; De Raedt, H.; Katsnelson, M. I. Optical conductivity of disordered graphene beyond the Dirac cone approximation. *Phys. Rev. B* **2011**, *84*, 195418.

(97) Viola, G.; Wenger, T.; Kinaret, J.; Fogelström, M. Graphene plasmons: Impurities and nonlocal effects. *Phys. Rev. B* **2018**, *97*, 085429.

(98) Aguillon, F.; Marinica, D. C.; Borisov, A. G. Plasmons in graphene nanostructures with point defects and impurities. *The Journal of Physical Chemistry C* **2021**, *125*, 21503–21510.

(99) Chen, Y.-C.; de Oteyza, D. G.; Pedramrazi, Z.; Chen, C.; Fischer, F. R.; Crommie, M. F. Tuning the Bandgap of Graphene Nanoribbons Synthesized from Molecular Precursors. *ACS Nano* **2013**, *7*, 6123–6128.

(100) Narita, A.; Wang, X.-Y.; Feng, X.; Müllen, K. New advances in nanographene chemistry. *Chem. Soc. Rev.* **2015**, *44*, 6616–6643.

(101) Talirz, L.; Ruffieux, P.; Fasel, R. On-Surface Synthesis of Atomically Precise Graphene Nanoribbons. *Advanced Materials* **2016**, *28*, 6222–6231.

(102) Chen, Z.; Narita, A.; Müllen, K. Graphene Nanoribbons: On-Surface Synthesis and Integration into Electronic Devices. *Advanced Materials* **2020**, *32*, 2001893.

(103) Meinzer, N.; Barnes, W. L.; Hooper, I. R. Plasmonic meta-atoms and metasurfaces. *Nature Photonics* **2014**, *8*, 889–898.

(104) Kravets, V. G.; Kabashin, A. V.; Barnes, W. L.; Grigorenko, A. N. Plasmonic Surface Lattice Resonances: A Review of Properties and Applications. *Chemical Reviews* **2018**, *118*, 5912–5951.

(105) Castellanos, G. W.; Bai, P.; Gómez Rivas, J. Lattice resonances in dielectric metasurfaces. *Journal of Applied Physics* **2019**, *125*, 213105.

(106) Soun, L.; Héron, S.; Ouazzani, H. E.; Fix, B.; Haïdar, R.; Bouchon, P. 4000-enhancement of difference frequency generation in a mode-matching metamaterial. *Opt. Express* **2020**, *28*, 27210–27222.

(107) Mikhailov, S. Theory of the nonlinear optical frequency mixing effect in graphene. *Physica E: Low-dimensional Systems and Nanostructures* **2012**, *44*, 924–927.

(108) Liu, S.; Vabishchevich, P. P.; Vaskin, A.; Reno, J. L.; Keeler, G. A.; Sinclair, M. B.; Staude, I.; Brener, I. An all-dielectric metasurface as a broadband optical frequency mixer. *Nature Communications* **2018**, *9*, 2507.

TOC Graphic